

# Normalizing Tumor Microenvironment Based on Photosynthetic Abiotic/Biotic Nanoparticles

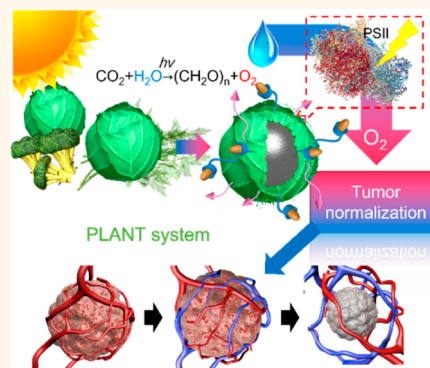
Diwei Zheng,<sup>§</sup> Bin Li,<sup>§</sup> Lu Xu, Qiu-Ling Zhang, Jin-Xuan Fan, Chu-Xin Li, and Xian-Zheng Zhang\*<sup>¶</sup>

Key Laboratory of Biomedical Polymers of Ministry of Education & Department of Chemistry, Wuhan University, Wuhan 430072, People's Republic of China

## Supporting Information

**ABSTRACT:** Tumor hypoxia has attained the status of a core hallmark of cancer that globally affects the entire tumor phenotype. Reversing tumor hypoxia might offer alternative therapeutic opportunities for current anticancer therapies. In this research, a photosynthetic leaf-inspired abiotic/biotic nanothylakoid (PLANT) system was designed by fusing the thylakoid membrane with synthetic nanoparticles for efficient O<sub>2</sub> generation *in vivo*. Under 660 nm laser irradiation, the PLANT system exhibited intracellular O<sub>2</sub> generation and the anaerobic respiration of the multicellular tumor spheroid was suppressed by PLANT as well. *In vivo*, it was found that PLANT could not only normalize the entire metabolic network but also adjust the abnormal structure and function of the tumor vasculature. It was demonstrated that PLANT could significantly enhance the efficacy of phototherapy or antiangiogenesis therapy. This facile approach for normalizing the tumor microenvironment will find great potential in tumor therapy.

**KEYWORDS:** thylakoid, oxygenation, tumor microenvironment, photocatalyst, cancer therapy



Tumors display significant variations in both physiological and biological properties of their extracellular microenvironments.<sup>1</sup> Among all these variations, hypoxia is a universal physiological feature of most solid tumors.<sup>2</sup> In general, the influence of hypoxia in biological properties of solid tumors is multifaceted. In one aspect, severe hypoxia would cause metabolic reprogramming (like anaerobic respiration) in tumor cells.<sup>3</sup> During this process, metabolites generated from anaerobic respiration could satisfy the bioenergetic requirement of tumor growth. Besides, some metabolites (especially lactate) are well known for their capacity in appropriating cellular redox status and offsetting reactive oxygen species (ROS)-dependent therapies.<sup>4</sup> In the other aspect, the complex behavior of tumor cells is also greatly influenced by tumor hypoxia. For example, tumor hypoxia is a powerful driving force in angiogenesis, and worse yet, pathological angiogenesis always leads to rapid tumor growth and deadly metastatic phenotype.<sup>5,6</sup> By reflecting all these massive roles in accelerating tumor progress and compromising treatment efficacy of various agents, normalizing the tumor microenvironment by reversing hypoxia was speculated to be a promising strategy.

In order to achieve the purpose of tumor normalization, a range of pioneer research studies were performed with biological or physical methods.<sup>7,8</sup> Evidence from genetically modified mice proved the enhancement of the therapeutic effect in various treatments by systematically normalizing the tumor microenvironment through tumor oxygenation concen-

tration elevation.<sup>9</sup> However, both the risk of insertional mutagenesis and the difficulty of systemic transfection greatly restricted the clinical applications of such tactics.<sup>10</sup> As a physical therapy, hyperbaric oxygenation was employed as a therapeutic adjunct to oxygenate arterial blood. It was expected to directly up-regulate the intratumoral O<sub>2</sub> pressure (PO<sub>2</sub>). Unfortunately, hyperbaric oxygenation displayed only very limited success in the clinic, and the existence of large holes (from 0.2 to 1.2 μm) in tumor vessel walls was considered to be a major reason preventing O<sub>2</sub> diffusion from vessels to the parenchyma.<sup>11</sup>

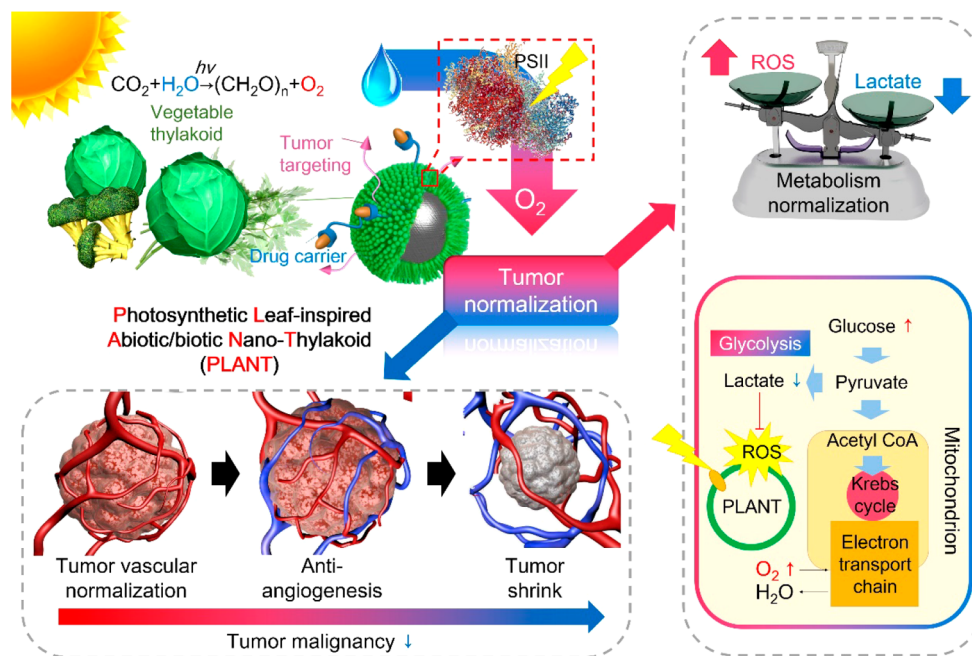
To date, nanomaterials are well known for passively accumulating within the solid tumor, and a series of nanomaterials were proposed to realize O<sub>2</sub> generation chemically. Unfortunately, the O<sub>2</sub> generation capacity mainly relied on H<sub>2</sub>O<sub>2</sub> decomposition (intracellular concentration <10 μM) or self-hydrolysis (e.g., CaO<sub>2</sub>).<sup>12–15</sup> Limited reactant concentration *in vivo* and poor controllability in space and time are still critical challenges. To address these challenges, constructing materials that could directly produce O<sub>2</sub> from inexhaustible raw materials *in vivo*, such as water, with a high controllability would be a perfect choice.<sup>16–18</sup> In nature, plants have evolved an elaborate oxygenic photosynthesis system in leaf cells to achieve high-efficiency photocatalyzed O<sub>2</sub> generation.<sup>19–21</sup> Inspired by such biochemical reactions in leaves, as shown in Scheme 1, we

Received: April 20, 2018

Accepted: May 23, 2018

Published: May 23, 2018

**Scheme 1.** Schematic diagram of the tumor normalization induced by the PLANT system. The versatile PLANT system was fabricated by fusing vegetable thylakoid with various nanoparticles. Under light irradiation, photosynthetic enzymes in PLANT catalyzed the water splitting reaction and produced  $O_2$  *in situ*. Functional patch molecules could be further integrated into the PLANT system *via* hydrophobic interactions. The rapid  $O_2$  generation triggered by PLANT was found to normalize the tumor microenvironment and systematically enhanced the therapeutic effect of antiangiogenesis therapy and photodynamic therapy.



designed a photosynthetic leaf-inspired abiotic/biotic nano-thylakoid (PLANT) system by fusing an  $O_2$ -generated thylakoid (Tk) membrane with synthetic nanoparticles to achieve efficient  $O_2$  production *in vivo*. Compared with traditional  $O_2$  generation materials such as  $CaO_2$  or  $MnO_2$ , it was found that PLANT exhibited significantly increased  $O_2$  production upon 660 nm laser irradiation. In a multicellular tumor spheroid (MTS) model, PLANT not only reversed the apparent tumor hypoxia but also restricted cell migration and inhibited anaerobic respiration. By using metabolomics analysis, it was demonstrated that PLANT could restore the oxygen supply and subsequently readjust the abnormal tumor microenvironment *in vivo*. In addition, the optically controlled tumor oxygenation material was combined with  $O_2$ -related therapy (e.g., phototherapy and antiangiogenesis therapy) for tumor treatment.

## RESULTS AND DISCUSSION

**Preparation of Tk Engineered Nanoparticles.** In this study, the Tk of spinach, lettuce, and cabbage were isolated with differential centrifugation methods (Figure 1a). As shown in Figure 1b, after the purification, protein bands in the 26–31 kDa region completely remained, and these bands were attributed to chlorophyll–protein complexes in light reactions,<sup>22</sup> whereas most of the other protein bands disappeared. TEM images of Tk are also shown in Figure S1. As shown in Figure 1c, it was found Tk obtained from spinach presented excellent  $O_2$  generation ability, and the high chlorophyll–protein complexes level in spinach leaves should be the main reason. Then, the natural Tk membrane was fused with various synthetic nanoparticles including Ag nanoparticles,  $SiO_2$  nanoparticles, and ZnO nanoparticles to obtain Ag@Tk (PLANT),  $SiO_2$ @Tk, and ZnO@Tk, respectively. As shown in Figure 1d, sizes of PLANT,  $SiO_2$ @Tk, and ZnO@Tk were

measured to be around 109 nm (PDI = 0.17), 114 nm (PDI = 0.06), and 232 nm (PDI = 0.17), respectively. Additionally, the high-resolution TEM also confirmed the formation of a Tk shell around various nanoparticles (Figure S1). UV–vis absorption spectra and zeta-potential also indicated the successful preparation (Figure S2). Since gold nanoparticles (AuNPs) could quench the fluorescence of chlorophyll when the distance between them was less than 10 nm, the fluorescence of Tk before and after coating AuNPs was measured (Figure 1e).<sup>23</sup> As shown in Figure 1f, the fluorescence decreased to one-seventh of its original intensity, which indicated the successful fusion of Tk and AuNP.

Subsequently, we observed that the  $O_2$  generation of Tk was improved with different levels after coating in different materials (Figure 1g). Herein, the possible mechanism of this phenomenon was speculated and schematically illustrated in Figure 1h. The conductive Ag nanoparticles could enhance the electron transfer rate, thus significantly increasing  $O_2$  generation in the beginning. Similarly, semiconductive ZnO could combine with the PSII to form an electron shuttle, and electrons produced by PSII would be accepted by the valence band of ZnO. As a consequence, ZnO@Tk also displayed a mild and enduring  $O_2$  generation. Meanwhile,  $SiO_2$ , with poor conductivity, showed limited effectiveness in improving the  $O_2$  production rate of Tk.<sup>24</sup> As shown in Figure 1i, we observed that attributed to the high efficiency of photosynthesis, PLANT ( $0.57 \text{ mmol g}^{-1} \text{ h}^{-1}$ ) produced a high amount of  $O_2$  within 6 min at levels of 4.0 times and 7.1 times higher than traditional  $O_2$  generation materials such as  $CaO_2$  ( $0.14 \text{ mmol g}^{-1} \text{ h}^{-1}$ ) and  $MnO_2$  ( $0.08 \text{ mmol g}^{-1} \text{ h}^{-1}$ ), respectively. Commonly, the  $PO_2$  in the  $O_2$ -rich tissues was about 20 mmHg, and  $O_2$  produced by PLANT, at a low concentration of  $2 \mu\text{g mL}^{-1}$ , was calculated to be about 38 mmHg after 5 min of irradiation. Thus, PLANT was expected to fully reverse the tumor

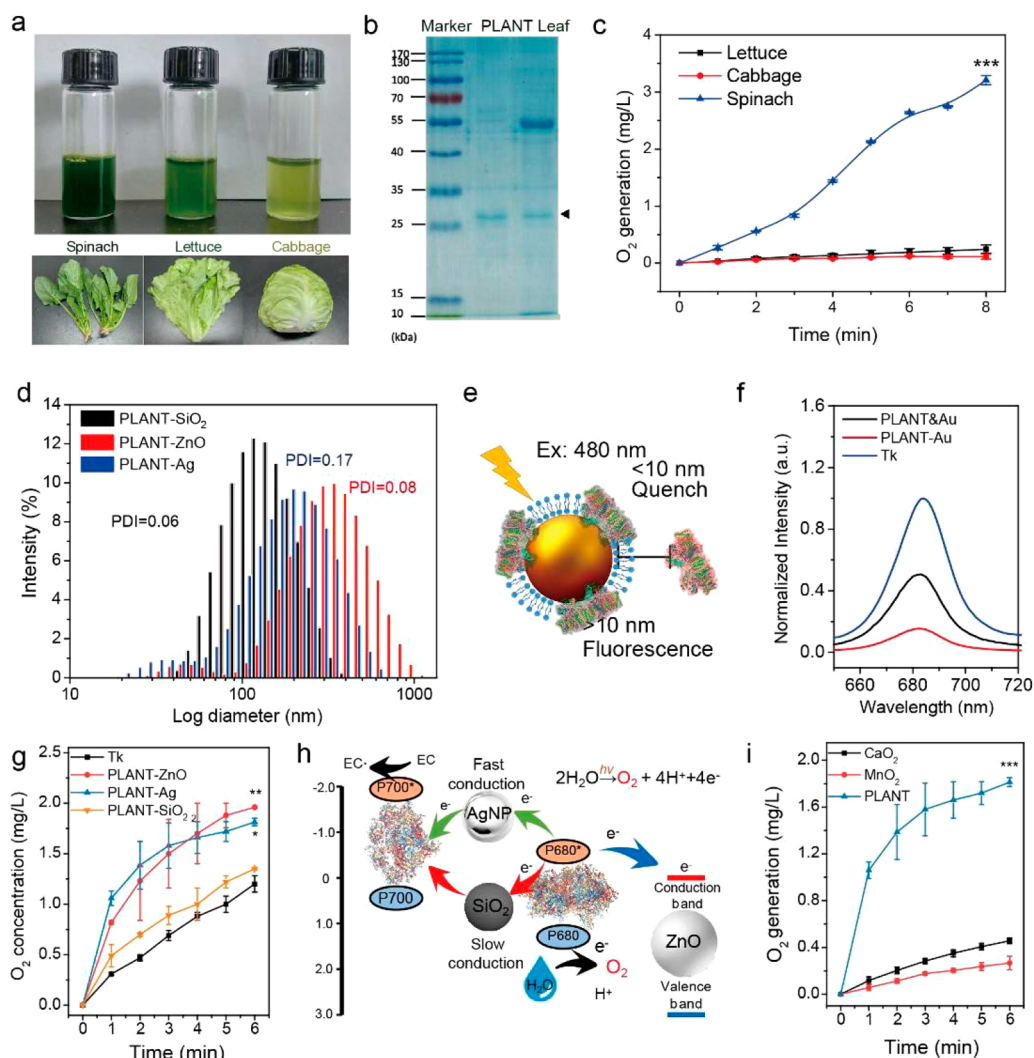


**Figure 1.** *In vitro* characterization of PLANT. (a) Images of Tk obtained from spinach, lettuce, and cabbage, respectively. (b) SDS-PAGE protein analysis of source spinach leaf homogenate and spinach Tk. (c) O<sub>2</sub> generation capacity of Tk isolated from spinach, lettuce, and cabbage leaves under 660 nm light irradiation. (d) Hydrodynamic sizes of PLANT-Ag, PLANT-ZnO, and PLANT-SiO<sub>2</sub>. (e) Schematic diagram of the distance-dependent fluorescence quench between AuNP and Tk. (f) Fluorescence quenching induced by Tk-coated AuNPs. The direct mixing of Tk and AuNP only induced minor fluorescence quench. (g) O<sub>2</sub> generation of PLANT-Ag, PLANT-ZnO, and PLANT-SiO<sub>2</sub>. (h) Schematic diagram of the enhanced O<sub>2</sub> generation mechanisms of PLANT. (i) O<sub>2</sub> generation capacity of PLANT, CaO<sub>2</sub>, and MnO<sub>2</sub>. Results are expressed as the mean  $\pm$  SD of at least three independent experiments measured in triplicate. \* $P < 0.05$ , \*\* $P < 0.01$ , \*\*\* $P < 0.001$ .

hypoxia.<sup>25</sup> Besides, as shown in Figure 2a, multifunctional components could be easily appended into the PLANT system to obtain an all-in-one platform.

***In Vitro* Tumor Normalization.** To demonstrate that PLANT treatment could fully reverse the hypoxia condition, herein, ROS-ID, a probe whose fluorescence could be quenched by O<sub>2</sub>, was used for indicating intracellular O<sub>2</sub> levels in the MTS model.<sup>26</sup> As shown in Figure 2b and Figure S3, increased red fluorescence was observed after the staining, and we found that CaO<sub>2</sub> and MnO<sub>2</sub> treatments did reduce the MTS hypoxia to a certain extent. However, this effect was not obvious as compared with PLANT-treated MTS. To further quantitatively analyze the O<sub>2</sub> production kinetics of PLANT in MTS, the MitoXpress-Xtra probe was used to measure the O<sub>2</sub> consumption rate *in situ*. As displayed in Figure 2c, CaO<sub>2</sub> treatment resulted in a slightly reduced O<sub>2</sub> consumption, and the enduring but inefficient O<sub>2</sub> generation feature conformed to the slow hydrolysis kinetics of CaO<sub>2</sub>. In contrast, MnO<sub>2</sub>-treated MTS exhibited a slightly increased O<sub>2</sub> concentration in

the very beginning. However, a rapid decrease of dissolved O<sub>2</sub> was observed as time progressed. This was attributed to the limited level of H<sub>2</sub>O<sub>2</sub> within the cytoplasm (<10  $\mu$ M), which acted as a raw material in MnO<sub>2</sub>-mediated O<sub>2</sub> generation, and this might greatly restrict the endurance of O<sub>2</sub> generation.<sup>27</sup> The same result could also be observed in a long-term 2D culture condition (Figure 2d). A rapid and enduring increase of the O<sub>2</sub> concentration in the PLANT-treated MTS was observed, which also proved its excellent O<sub>2</sub> production ability.

Herein, the glucose consumption and lactate accumulation rates were used to determine the rate of glycolysis.<sup>28</sup> As shown in Figure 2e, in PLANT-treated MTS, the glucose consumption within 60 h decreased by 41.3%, whereas MnO<sub>2</sub> and CaO<sub>2</sub> treatments only inhibited 3.4% and 9.2% of glucose consumption, respectively. A considerable lactate accumulation could also be observed in the phosphate-buffered saline (PBS) control. After MnO<sub>2</sub> or CaO<sub>2</sub> treatment, the lactate generation was slightly reduced. However, PLANT was found to inhibit 56.7% of lactate generation (Figure 2f). Together, these results

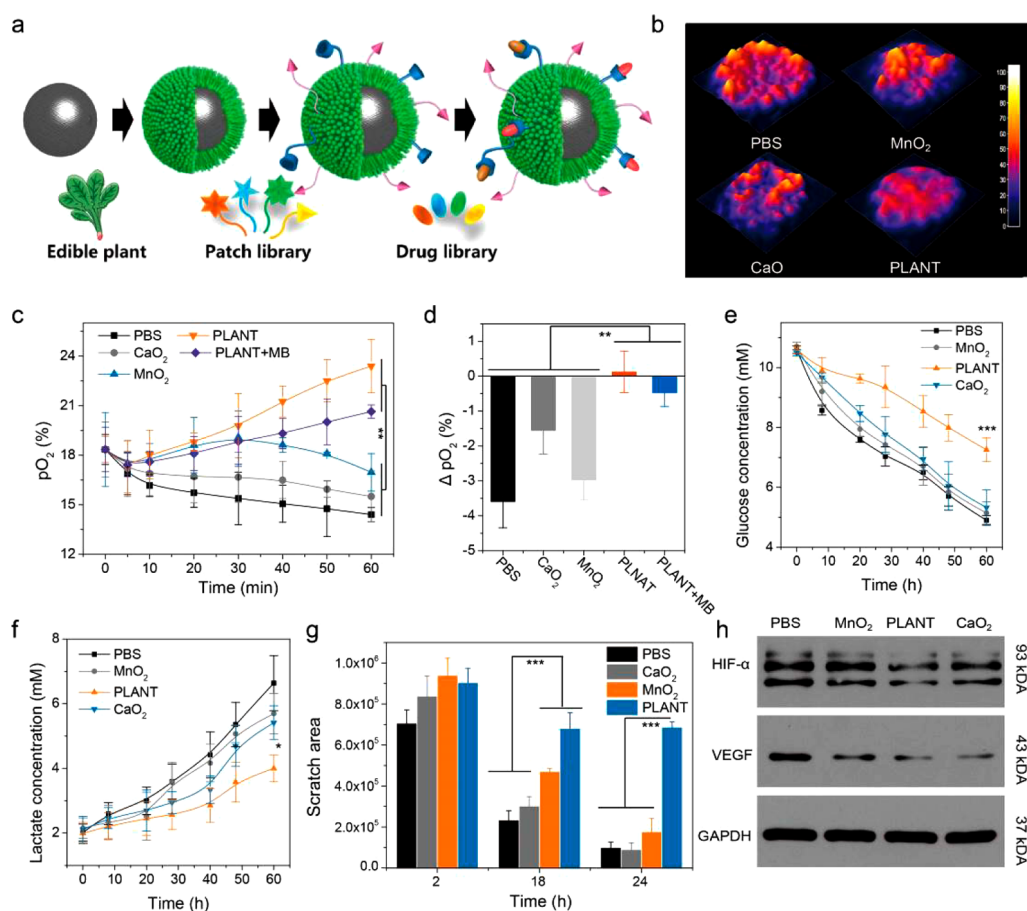


**Figure 2.** *In vitro* study of PLANT in modulating cell metabolism and behavior. (a) Preparation of PLANT including three key steps: isolation of Tk from edible vegetables to coat nanoparticles; selecting molecules from a patch library to functionalize Tk-coated nanoparticles; carrying drug molecules *via* a host–guest interaction. (b) Surface plot images and 2D fluorescence images of ROS-ID-stained CT26 MTS after 4 h of co-incubation with phosphate-buffered saline (PBS),  $\text{MnO}_2$ ,  $\text{CaO}_2$ , and PLANT. (c) MitoXpress-Xtra probe for monitoring the extracellular  $\text{O}_2$  concentration of PBS-,  $\text{MnO}_2$ -,  $\text{CaO}_2$ -, and PLANT-treated CT26 MTS in real time. (d) MitoXpress-Xtra probe for monitoring the extracellular  $\text{O}_2$  concentration of CT26 cells 24 h after PBS,  $\text{MnO}_2$ ,  $\text{CaO}_2$ , and PLANT treatment. (e) Glucometer for monitoring the glucose concentration of PBS,  $\text{MnO}_2$ ,  $\text{CaO}_2$ , and PLANT treatment in real time. (f) Lactate assay for monitoring the lactate concentration of PBS,  $\text{MnO}_2$ ,  $\text{CaO}_2$ , and PLANT treatment in real time. (g) Migration- and invasion-preventing ability of various  $\text{O}_2$  generation materials in inhibiting CT26 cell migration was evaluated by a wound healing assay. The wound width was imaged and quantitatively analyzed after PBS,  $\text{MnO}_2$ ,  $\text{CaO}_2$ , and PLANT treatments. (h) Western blot demonstrating decreased HIF- $\alpha$  and VEGF levels after various PBS,  $\text{MnO}_2$ ,  $\text{CaO}_2$ , and PLANT treatments. Results are expressed as the mean  $\pm$  SD of at least three independent experiments measured in triplicate. \* $P < 0.05$ , \*\* $P < 0.01$ , \*\*\* $P < 0.001$ .

suggested that the oxygenation induced by PLANT could switch anaerobic respiration to mitochondrial respiration and thereby might normalize the tumor metabolism *in vitro*. Subsequently, the effect of PLANT in modulating cell behavior was further studied. Herein, by using a wound healing assay, we found that PLANT could effectively suppress the cancer cell migration *in vitro* (Figure 2g).<sup>29</sup> We further analyzed the expression of hypoxia-associated proteins after  $\text{CaO}_2$ ,  $\text{MnO}_2$ , and PLANT treatments. As shown in Figure 2h, a marked decrease of hypoxia-inducible factor  $\alpha$  (HIF- $\alpha$ ) and vascular endothelial growth factor (VEGF) was observed after PLANT treatment.

**Metabonomics Analysis.** After confirming the *in vitro* biological effect of PLANT, we further explored the influence of PLANT in xenograft-bearing mice. Specifically, we performed a gas chromatography–mass spectrometry (GC-MS)-based metabolomic analysis for evaluating the regional and global effects of PLANT (Figure S4).<sup>30</sup> Herein, we identified 131 differential metabolites with the rate of change  $>50\%$  and  $P$

value  $<0.05$ . As shown in Figure 3a and Figure S5, metabolites could be subjected to unsupervised horizontal clustering, and this result confirmed a clear separation of samples after treatment with different methods. To screen the most important variable among all differential metabolites, Hotelling's  $T^2$  statistics was performed. Herein, the contribution of an individual variable to Hotelling's  $T^2$  statistics is listed in Figure 3b and Figure S6. Among all detected metabolites, lactic acid, yielding the highest Hotelling's  $T^2$  score, was considered to be the most important differential metabolite. Then, principal component analysis (PCA) showed that the metabolites in PLANT-treated mice tumors were highly distinct from the PBS groups in general (Figure 3c).

Subsequently, the Reactome data model was used to investigate diverse events and bioreactions in the mice tumors after PLANT treatment.<sup>31</sup> Herein, the reaction network of 26 top-level processes such as signal transduction, metabolism, disease, and transport of small molecules is displayed in Figure S7. As shown in Figure 3d, metabolism processes showed the

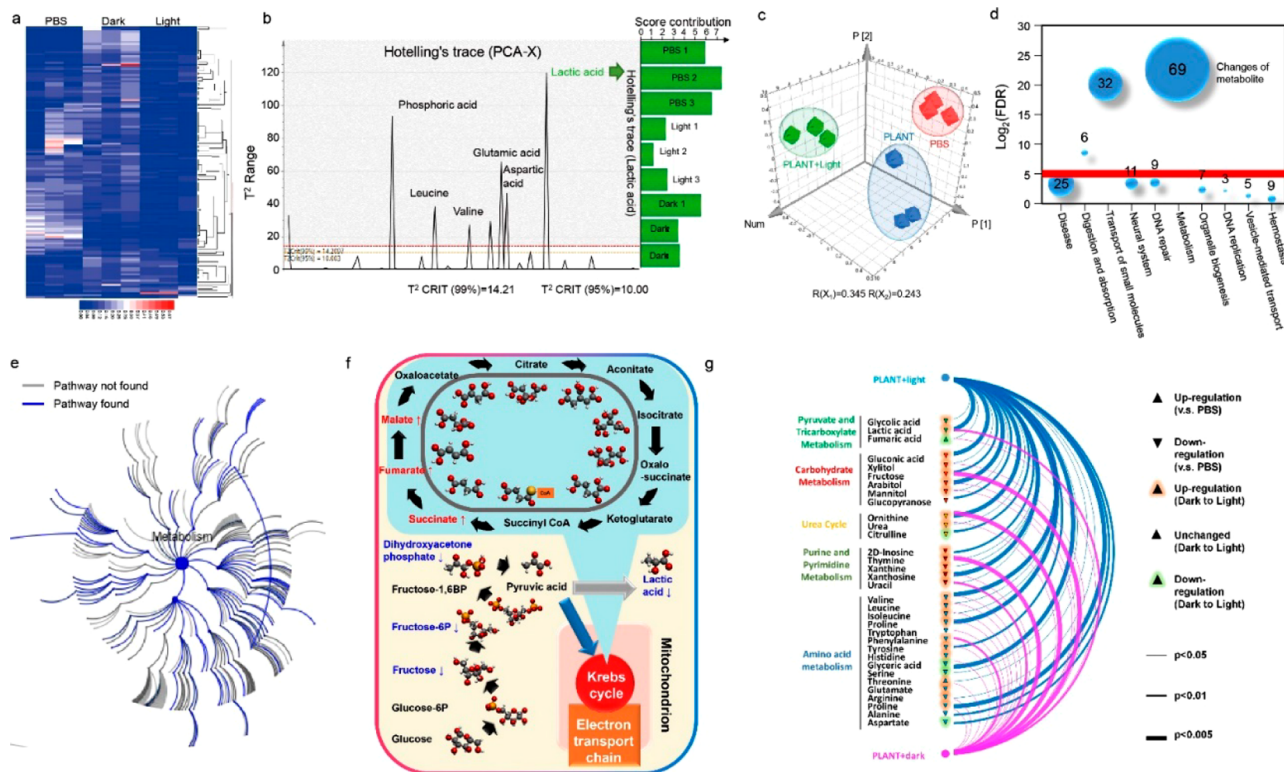


**Figure 3.** Metabonomics study of PLANT-treated CT26 tumors. (a) Heat map representation and cluster analysis of significantly difference in metabolites (hypergeometric test) in mice tumors 24 h after PBS, PLANT + light, and PLANT + dark treatments. (b) Hotelling's trace multivariate T test of all differential metabolites.  $T^2$  statistics with 95% and 99% confidence regions were calculated based on all differential metabolites. The score contribution of metabolite with the highest  $T^2$  score (lactic acid) is displayed in the right histogram. (c) Principal component analysis (PCA) score plot of the metabolites with significant differences in mice tumors. (d) A total of 131 metabolites were identified as differential metabolites between the PBS group and PLANT + light group. Circle diameters represent the number of metabolites in each pathway. (e) Reaction map of the cell metabolism process annotated in the Reactome database. (f) Schematically illustrated capacity of PLANT in inhibiting anaerobic respiration and enhancing aerobic respiration, thereby normalizing the tumor metabolism. (g) Arc plot of significant differential metabolites after treatment showing significant correlation with carbohydrate metabolism, amino acid metabolism, and nucleic acid metabolism across the PLANT-treated CT26 tumor with (blue) or without (violet) light irradiation.

minimum false discovery rate (FDR) values and the maximal variables, and we found that PLANT + light treatment influenced 29.0% of the reactions (found: 593; total: 2045) in the network of metabolism (Figure 3e). This result strongly indicated that most of the differential metabolites involved in PLANT treatment were contained in metabolism processes. Among all downstream pathways of metabolism processes, we noticed that the pathway of pyruvate metabolism and the citric acid (TCA) cycle displayed a significant change ( $P = 3.77 \times 10^{-4}$ , Figure 3f). Down-regulation of glycolysis-associated metabolites such as fructose, fructose-6-phosphate, and dihydroxyacetone phosphate was found. Notably, increased metabolites associated with the TCA cycle (e.g., malate, fumarate, and succinate) were identified after PLANT treatment. Thus, it was evidenced that PLANT could normalize the tumor glucose metabolism *in vivo*. Above all, PLANT treatment was observed to induce global changes among various bioprocesses, including metabolites associated with amino acids, nucleobases, and nucleotides (Figure 3g). The large-scale decrease of these tumor-related metabolites proved that PLANT was able to induce tumor normalization and thereby accelerate other cancer therapies.

**In Vivo Remolding of Tumor Microenvironment.** To confirm the tumor-targeting capacity of folic acid, PLANT with or without folic acid was injected into CT26 tumor bearing Balb/C mice, respectively. As shown in Figure 4a, after the i.v.

injection of PLANT, the red fluorescence intensity increased as time progressed. PLANT without folic acid showed poor tumor accumulation as compared with PLANT. This result was also confirmed by using 3D reconstructed fluorescence imaging/microcomputed tomography ( $\mu$ -CT) imaging and *ex vivo* fluorescence imaging. Furthermore, CLARITY technology, a tissue clearing method, was performed to achieve the 3D high-resolution imaging of tumors at a subcellular level (Figure S8).<sup>32</sup> As shown in Figure 4b, most of the PLANT fluorescence was located at the edge of the tumor, but there still existed some red fluorescence in the center of the mouse tumor. As shown in Figure 4c and Figure S9c, 3D fluorescence imaging of the tumor tissue also revealed that the PLANT was distributed throughout the xenograft.

Besides, some important blood biochemistry and hematologic indexes of mice after i.v. injection with PLANT were also analyzed to reveal its high biocompatibility (Figure S9d–g). A pharmacokinetics study proved the satisfactory circulation ability of PLANT. Immunoglobulin E measurement also revealed that PLANT itself is nonallergic to mice.

Subsequently, the biological effect of PLANT in remolding the tumor environment was studied. First, the XenoLightRe-diject2-DG 750 (NIR-2DG) probe was used to measure the hyperglycolytic Warburg effect within tumors.<sup>33</sup> As shown in Figure 4d, in the PBS control, a boosted amount of NIR-2DG probe was accumulated in the tumor parenchyma, and this

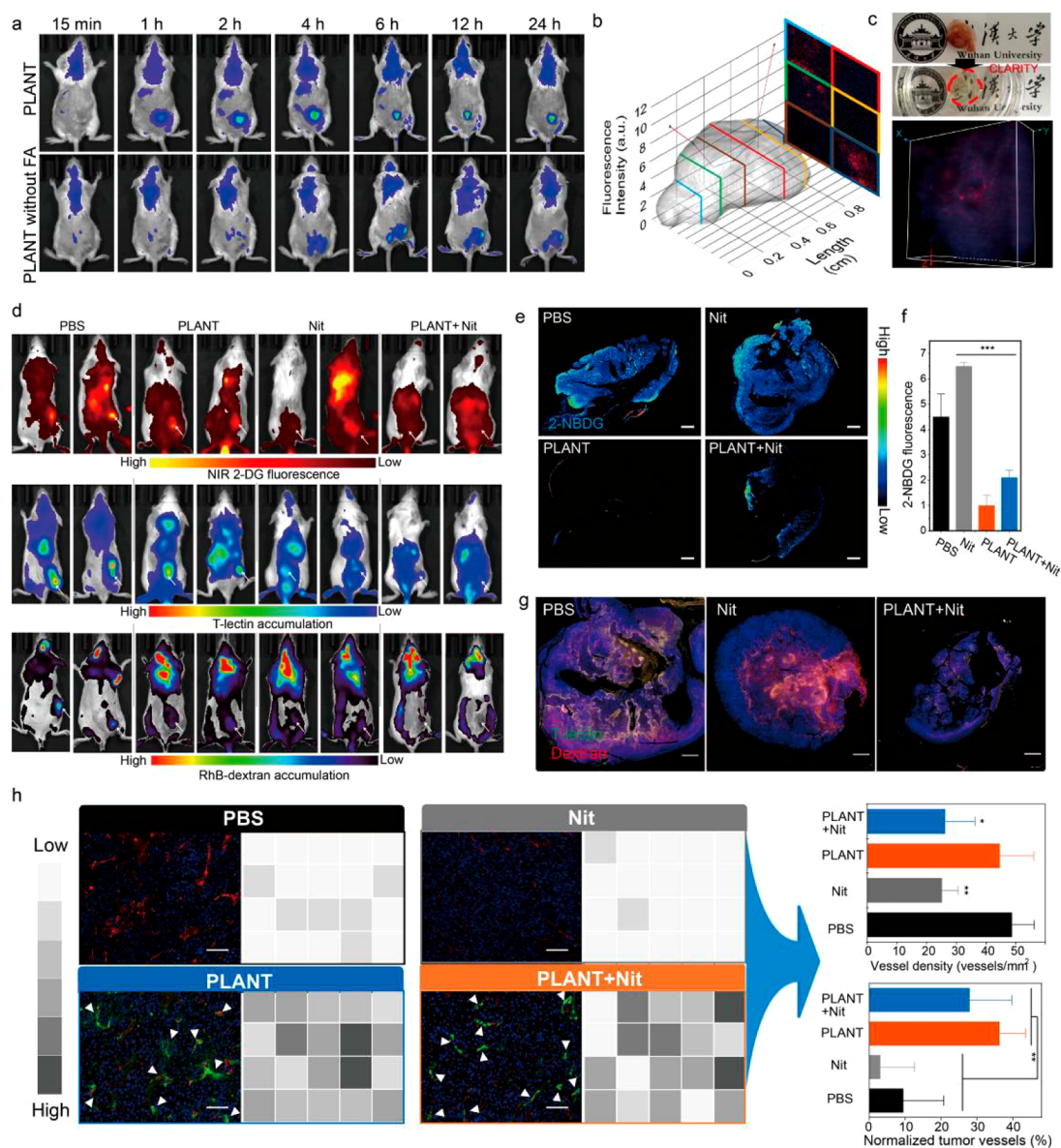


**Figure 4.** *In vivo* tumor targeting and biocompatibility of PLANT. (a) *In vivo* fluorescence imaging at different time points after i.v. injection of PLANT (top) and PLANT without folic acid (below), respectively. (b)  $\mu$ -CT-scanned whole tumor model and transverse CT26 tumor sections of PLANT after targeting. Images of each section were acquired using a fluorescence optical microscope. Fluorescence intensity of PLANT at different depths of the tumor was analyzed and displayed with a semiquantitative depth–fluorescence intensity curve. (c) Images of tumor tissues ( $1\text{ mm} \times 1\text{ mm} \times 250\text{ }\mu\text{m}$ ) before and after CLARITY treatment. (d) XenolightRediject 2-DG 750, Cy7-conjugated T-lectin, and Rhodamine B-conjugated dextran for real-time monitoring of the tumor glucose metabolism level, angiogenesis process, and tumor vessel leakage at the 10th day during various treatments. (e) False color fluorescent mapping of 2-NBDG distributions among the tumor tissue 48 h after treatment with nintedanib (Nit), PLANT, and PLANT + Nit (scale bar:  $1000\text{ }\mu\text{m}$ ). (f) Semiquantitative analysis of 2-NBDG fluorescence intensity within the tumor. (g) Microdistributions of T-lectin (combined with neovessels) and dextran (leakage from abnormal tumor vessels) after Nit, PLANT, and PLANT + Nit treatments (scale bar:  $1000\text{ }\mu\text{m}$ ). (h) Immunofluorescence images of  $\alpha$ -SMA and CD31 of tumors after treatment with Nit, PLANT, or PLANT + Nit and semiquantitative analysis of vessel density in mouse tumors or percentage of  $\alpha$ -SMA-covered CD31 expressed vascular endothelial cells (scale bar:  $100\text{ }\mu\text{m}$ ). Heat map analysis of normalized vessel distribution of Nit-, PLANT-, and PLANT + Nit-treated tumors. Results are expressed as the mean  $\pm$  SD of at least three independent experiments measured in triplicate. \* $P < 0.05$ , \*\* $P < 0.01$ , \*\*\* $P < 0.001$ .

result indicated the existence of hypermetabolism within tumors. In contrast, we observed that both PLANT treatments could partly reverse the abnormal tumor glycometabolism. Herein, nintedanib (Nit), a tyrosine kinase inhibitor of VEGF receptor, was used as a control, and we found that PLANT could reduce the high glucose metabolism level triggered by Nit. Furthermore, Cy7-conjugated tomato lectin (T-lectin) was used to mark the abnormal neovasculature. We found that

PLANT treatment could also slightly reduce the neovascular density.<sup>34</sup> Besides, upon injection of rhodamine B-conjugated dextran 70, both the *in vivo* and *ex vivo* fluorescence imaging decreased that PLANT treatment markedly decreased the extravasation of dextran from leaky tumor vessels.<sup>35</sup>

Then, by administration of fluorescent deoxyglucose analog (2-NBDG), specific glucose consumption within the tumor parenchyma was visualized. Figure 4e and f present the

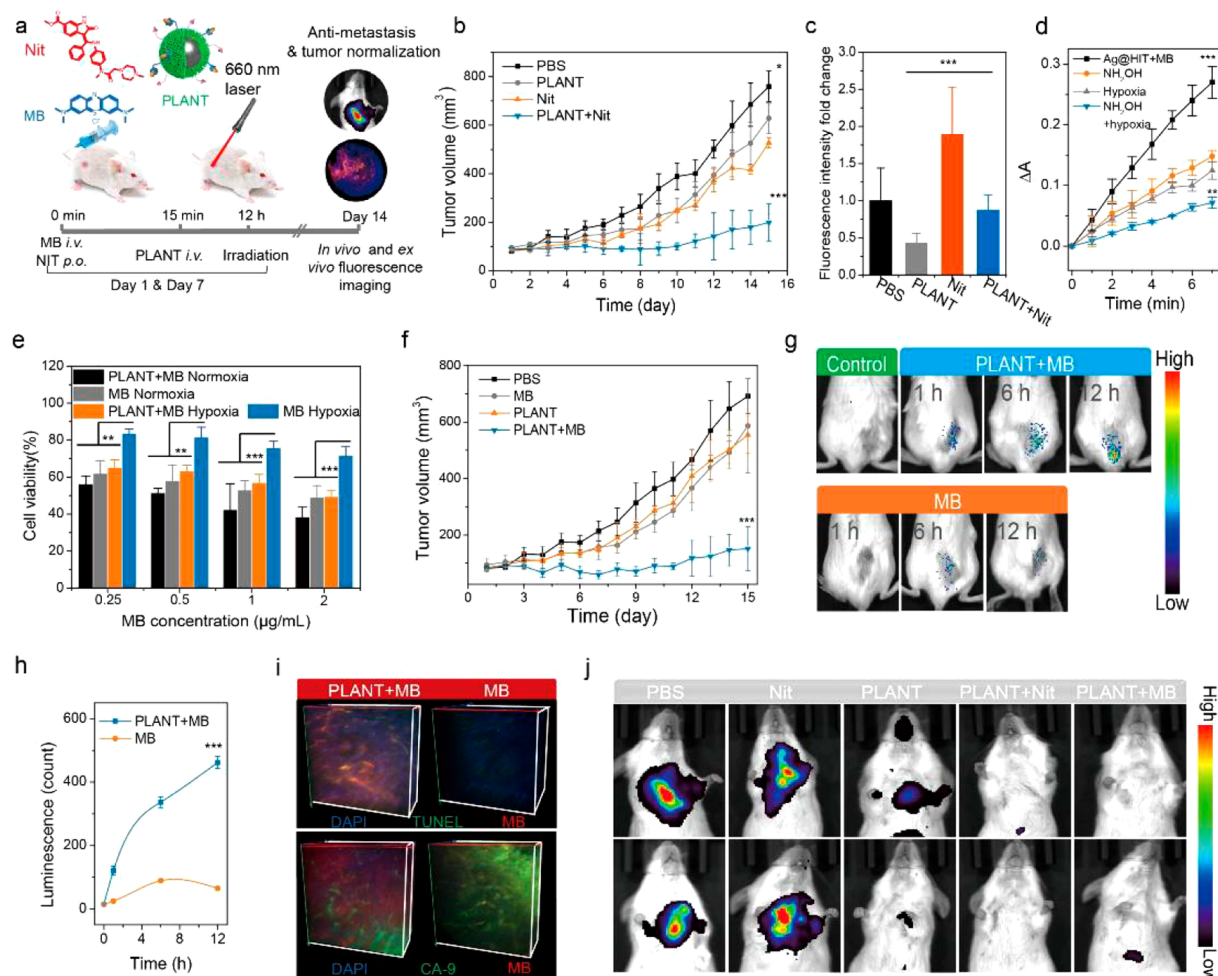


**Figure 5.** *In vitro* and *in vivo* study of PLANT in enhancing PDT and antiangiogenic therapy. (a) Schematic diagram of the *in vivo* therapy. For each group, Nit, PLANT, or PLANT + Nit was injected into tumor-bearing mice. At 24 h after injection, mice in the PLANT and PLANT + Nit groups were irradiated with a 660 nm laser ( $155 \text{ mW cm}^{-2}$ ) for 2 min. (b) Primary tumor volume curve following Nit, PLANT, and PLANT + Nit treatments,  $n = 5$ . (c) MitoXpress-Xtra probe for semiquantitative monitoring of the intratumoral  $\text{O}_2$  level after Nit, PLANT, and PLANT + Nit treatments. (d) Imidazole/4-nitrosodimethylaniline assay for evaluating the PLANT enhancement of the ROS generation of MB. (e) Cell viability assay of CT26 MTS after treatment with PLANT + MB and free MB. The addition of lactate (25 mM) could suppress the therapeutic effect of PDT. (f) Primary tumor volume curve following MB, PLANT, and PLANT + MB ( $n = 6$  for each group) treatments. (g, h) Oxidative stress responsive plasmid transfected CT26 tumor bearing mice for real-time illustration of the *in vivo* ROS generation kinetics of PLANT + MB. At 24 h after the injection, a 660 nm laser irradiation was performed. (i) 3D fluorescence imaging for visualizing the increased anticancer efficiency of PDT and tumor hypoxia reversion after PLANT treatment in tumor tissues with a size of  $1 \text{ mm} \times 1 \text{ mm} \times 250 \mu\text{m}$ . (j) *In vivo* bioluminescence imaging of luciferase-expressed CT26 tumor lung metastasis for Nit, PLANT, and PLANT + MB treatment groups at the 10th day. Results are expressed as the mean  $\pm$  SD of at least three independent experiments measured in triplicate. \* $P < 0.05$ , \*\* $P < 0.01$ , \*\*\* $P < 0.001$ .

representative 2-NBDG images of PBS-, Nit-, PLANT-, and PLANT + Nit-treated tumors.<sup>36</sup> Herein, we found that Nit treatment aggravated the tumor glycolysis. However, the addition of PLANT treatment could normalize the tumor glycometabolism, as markedly reduced 2-NBDG fluorescence was observed in PLANT + Nit-treated tumors. Additionally, the down-regulation of glycolysis-associated enzymes and glucose transporter proteins-1 (GLUT-1) after PLANT treatment was also found (Figure S10). Besides, Figure 4g also indicates that PLANT treatment could promote the tumor vascular maturity. Then, immunofluorescent staining of CD31 and HIF- $\alpha$  revealed that both tumor vessel density (CD31 level) and tumor parenchyma hypoxia (HIF- $\alpha$  level) were significantly decreased after PLANT treatment (Figure S11e).

Commonly, normal vessels are always covered with a layer of mural cells, and the existence of this structure can make vessels

more stable, tight, and mature. A marker of mature vascular epithelial cells,  $\alpha$ -smooth muscle actin ( $\alpha$ -SMA), was used to stain the mural cell layer. As shown in Figure 4h, most CD31-expressed vessels were covered with  $\alpha$ -SMA-expressed mural cells in PLANT-treated tumors. Hence, this result indicated that the oxygenation of PLANT could successfully normalize the vessel. Quantitatively, PLANT treatment could significantly normalize tumor vessels (pericyte-covered vessels:  $36.2 \pm 2.0\%$  in PLANT versus  $9.4 \pm 9.8\%$  in PBS, Figure 4h). Overall, these results indicated the high performance of PLANT remodeling and normalizing of the tumor microenvironment.

**PLANT Promotes Antiangiogenic/Photodynamic Therapy.** As we know, tumor hypoxia is a main side effect that reduces the outcomes of other therapies and promotes tumor aggressiveness.<sup>37</sup> To prove the therapeutic potential of PLANT, the *in vivo* therapeutic effects of PLANT, Nit, and

PLANT + Nit were studied in CT26 tumor bearing Balb/c mice (Figure 5a). As shown in Figure 5b, limited therapeutic outcomes were observed in PBS-, PLANT-, and Nit-treated mice, whereas the combination of PLANT and Nit was found to inhibit 84% of tumor growth. Subsequently, in histology analysis, the satisfactory therapeutic effect of PLANT + Nit was proved (Figure S11). By using a MitoXpress Intra probe, we noticed that PLANT treatment could significantly reduce tumor hypoxia *in vivo* (Figure 5c).

In a further step, the effect of PLANT in enhancing PDT was tested. As shown in Figure 5d, first, we observed that the ROS generation of methylene blue (MB) could be significantly enhanced by PLANT both in hypoxic and in normoxic environments. The addition of an electron transfer inhibitor ( $\text{NH}_2\text{OH}$ ) could inhibit the sensitization of PLANT. As shown in Figure 5e, for PLANT-treated CT26 cells, >50% of cancer cells could be inhibited by MB in the hypoxic environment. Therefore, we demonstrated that PLANT could strongly enhance PDT efficiency in both normoxic and hypoxic cancer cells. Apart from this mechanism, lactate derived from the anaerobic respiration of cancer cells was also correlated with the resistance of ROS-dependent therapies.<sup>38</sup> In an MTS model, we also proved that the generation of lactic acid was a dominant factor in suppressing the therapeutic effect of PDT (Figure S11c). Nevertheless, PLANT treatment could enhance the cytotoxicity of MB by about 36%. By using an intracellular ROS probe, DCFH-DA, and a hypoxia probe, ROS-ID, we also observed that by treating with PLANT tumor hypoxia could be reversed, and evident ROS generation could be triggered (Figure S12).

Then, we conducted an *in vivo* anticancer therapy in CT26 tumor bearing Balb/C mice. As shown in Figure 5f, only one dose of PLANT together with MB showed a tumor inhibition rate of 77%, whereas free MB showed a low tumor inhibition rate of 15%. This situation was also verified by the representative tumor image and pathological section after 15 days of treatments.

To prove that the enhanced therapeutic effect of MB was attributed to the  $\text{O}_2$  generation capacity of PLANT, we designed a plasmid containing oxidative stress responsive elements (OREs) that could drive the expression of luciferase proteins (Figure S12).<sup>39</sup> After revealing the oxidative stress responsiveness of transfected CT26 cells (CT26<sup>OR</sup>) *in vitro*, models of CT26<sup>OR</sup> cells xenografted Balb/C mice were prepared. As shown in Figure 5g,h, before the laser irradiation, no bioluminescence in the mice tumor could be observed. However, after irradiation, a boosted amount of bioluminescence was detected within the PLANT group. The oxidative stress in PLANT-treated tumors was kept at a high level, whereas MB only showed a limited response. We also confirmed the satisfactory tumor inhibiting effect of PLANT by using CLARITY treatment. As shown in Figure 5i, we found that a mass of cancer cells underwent apoptosis. In addition, red fluorescence from material and green fluorescence of apoptotic cancer cells were well overlapped. This result clearly revealed that apoptotic cancer cells within tumors were indeed killed by PLANT + MB. After free MB treatment, CA-9 location and MB distribution were merged. This result suggested that MB-mediated PDT caused serious tumor hypoxia, whereas less fluorescent overlap in PLANT-treated mice was observed.

**Tumor Normalization Prevents Tumor Metastasis.** Fighting against metastatic tumors was also an equally important assignment in current comprehensive cancer

therapies.<sup>40–43</sup> Herein, we explored whether intratumoral oxygenation triggered by PLANT could inhibit the tumor metastasis. After 14 days of various treatments in luciferase-expressed CT26 tumor bearing mice, peripheral blood of tumor-bearing mice was collected, and circulating tumor cells were counted by measuring the bioluminescence intensity. As shown in Figure S11j, we found that PLANT treatment could reduce 57% of bioluminescence intensity in peripheral blood. Subsequently, bioluminescence of the luciferase-expressing CT26 cells in mouse lung was measured. As shown in Figure 5j and Figure S11k, only in treatments containing PLANT were there fewer metastatic cells, whereas in mice untreated or exclusively treated with Nit, serious lung metastasis appeared.

## CONCLUSIONS

In summary, we reported on the design, preparation, and therapeutic effects of the  $\text{O}_2$ -generating PLANT system for achieving tumor normalization. *In vitro* investigations demonstrated that PLANT could produce sufficient  $\text{O}_2$  that could theoretically reverse the tumor hypoxia. By using an MTS model, it was indicated that PLANT could not only reverse the tumor hypoxia but also normalize tumor cells both in metabolism and in behavior. Besides, by using fluorescence probes and the CLARITY technology, the satisfactory *in vivo*  $\text{O}_2$  generation capacity of PLANT was also proved. After confirming the detailed mechanism of oxygenation-enhanced tumor normalization, improved therapeutic outcomes were observed in the experiments of PLANT combining with  $\text{O}_2$  relevant PDT or antiangiogenesis therapy *in vitro* and *in vivo*. Obviously, PLANT will overcome the last hurdle of *in vivo* oxygenation therapy and may shed light on the  $\text{O}_2$ -supporting anticancer treatments.

## METHODS

**Synthesis of Ag Nanoparticles.** A 20 mg amount of  $\text{AgNO}_3$  was dissolved in 100 mL of deionized (DI) water and then heated to 100 °C. A 2 mL sample of 1% sodium citrate solution was added dropwise. The reaction was kept at 100 °C for 1 h. After that, AgNP was then centrifuged and washed with DI water three times. To avoid the oxidation reaction, the as-prepared AgNPs should be used as soon as possible.

**Isolation of Thylakoid.** First, 50 mM HEPES buffer (pH = 7.6) containing 5 mM  $\text{MgCl}_2$ , 50 mM NaCl, and 0.3 M sucrose was prepared. Different leaves were then homogenized in the ice-cold buffer with a high-speed juice extractor (Aux HX-PB1052). The homogenate was then filtrated through four layers of cheesecloth, and the filter liquor was centrifuged at 600g for 5 min. Subsequently, the supernatant was centrifuged for another 10 min at 1500g. The pellet was resuspended in osmotic shock buffer (10 mM HEPES, pH 7.6, 10 mM NaCl, and 5 mM  $\text{MgCl}_2$ ) for 20 min. The suspension was then centrifuged for 20 min at 2500g. The pellet was carefully collected and resuspended in a potassium ferricyanide (1 mM)-containing osmotic shock buffer. The whole process should be performed on ice. The Tk solution with a chlorophyll concentration of 0.8 mg  $\text{L}^{-1}$  was stored for further use.

**Preparation of Tk-Coated Nanoparticles.** Tk was physically extruded through 800 nm porous polycarbonate membranes in 11 passes in an Avanti mini extruder. Then, 1 mL of ZnO nanoparticles, AgNPs, or  $\text{SiO}_2$  nanoparticles (1 mg  $\text{mL}^{-1}$ , respectively) was mixed with 1 mL of extruded membrane solution and coextruded for 11 passes through a 400 nm porous polycarbonate membrane, respectively, to obtain Tk-coated nanoparticles.

**Self-Assembly of PLANT.** A 2 mL amount of Tk-coated AgNPs was mixed with 3 mg of SA- $\beta$ -CD (0.002 mmol) and 3 mg of DSPE-PEG-FA. After stirring for 6 h at room temperature, the product was centrifuged and washed three times by DI water and then redissolved

in 2 mL of PBS (pH 7.4). To prepare MB plugging PLANT, 2 mg of MB (0.006 mmol) was mixed with 2 mL of the above PLANT solution, and the mixture was stirred for 2 h. Subsequently, the mixture was centrifuged and washed three times by DI water and redissolved in 2 mL of PBS.

**O<sub>2</sub> Generation Assay.** A 1 mL amount of Tk solution or diverse Tk-coated nanoparticle solutions were mixed with 1 mL of PBS, respectively. Then the solution was illuminated under an LED light (660 nm, 18 W) for 8 min, and a JPSJ-605F oxygen dissolving meter (INESA Scientific Instrument Co., Shanghai) was used to measure the O<sub>2</sub> generation in real time. Specially, a Tk solution with 1 mM K<sub>3</sub>Fe(CN)<sub>6</sub> was measured as a control.

**Multicellular Tumor Spheroid Model.** Briefly, a 96-well plate was coated with 1% agarose gel. After the solidification, CT26 cells were seeded with a density of 1000 cells per well, and cells were cultured at 37 °C for 7 days. The uniform and complete spheroids were used for further studies. For *in vitro* O<sub>2</sub> generation study, MnO<sub>2</sub> (100 μg mL<sup>-1</sup>), CaO<sub>2</sub> (100 μg mL<sup>-1</sup>), and PLANT (with a photosynthetic protein content of 2 μg mL<sup>-1</sup>) were added into the MTS model. Four hours after the co-incubation, the intracellular O<sub>2</sub> concentration was visualized with ROS-ID reagent. MitoXpress-Xtra probe (Luxcel Biosciences, Ireland) was also used to monitor the extracellular O<sub>2</sub> concentration in real time. MitoXpress-Xtra probe (100 nM) and various materials were added into the 96-well plates. Then 100 μL of mineral oil was applied to seal the wells, and measurements were carried out with a SpectraMax i3x multimode detection platform.

**Metabonomics.** Female Balb/C mice were subcutaneously injected with 100 μL of CT26 cells (1 × 10<sup>6</sup> cells per mouse). When the average tumor volume reached 200 mm<sup>3</sup>, 100 μL of PBS or PLANT (4 mg mL<sup>-1</sup>, in 100 μL of PBS) was *i.v.* injected into mice. Twenty-four hours after the injection, 660 nm laser irradiation (150 mW cm<sup>-2</sup>, 5 min) was performed. At 12 h after the irradiation, CT26 tumors were collected. A 10 mg amount of tumor samples was then added into 1000 μL of extractant (acetonitrile/2-propanol/water, 3:3:2, *v:v:v*). Then, tumor samples were treated with ultrasonic irradiation for 1 min. The mixture was centrifuged for 5 min at 13 000 rpm. A 20 μL amount of 3 mg mL<sup>-1</sup> myristic acid-*d*<sub>27</sub> was mixed with 800 μL of supernate. The mixture was blown dry with nitrogen gas followed by adding 20 μL of methoxyamine hydrochloride/pyridine (40 mg mL<sup>-1</sup>) or 90 min at 30 °C. A 90 μL amount of *N*-methyl-*N*-(trimethylsilyl) trifluoroacetamide with 1% trimethylchlorosilane (MSTFA + 1% TMCS) was added and co-incubated for 30 min at 37 °C. After 5 min of centrifugation, 80 μL of supernatant was collected for GC/MS analysis. GC/MS measurements were performed on an Agilent 7890 GC-Agilent 5975c inert MSD with a triple-axis detector. A commercial GC capillary column (Agilent ZORBAX DB5-MS, 30 m length × 0.25 mm i.d. × 0.25 μm) (Agilent Technology) was used for comparison of GC separation. Principal component analysis was measured with Simca P 13.0 software.

***In Vivo* Anticancer Therapy.** Female Balb/C mice were subcutaneously injected with 100 μL of CT26 cells (1 × 10<sup>6</sup> cells per mouse). When the average tumor volume reached 100 mm<sup>3</sup>, mice were divided into four groups randomly (*n* = 6). A 100 μL amount of PBS, PLANT + MB, or MB (with an MB dose of 5 mg kg<sup>-1</sup>) was *i.v.* injected into CT26 tumor bearing mice, respectively. For Nit treatment, Nit (125 mg kg<sup>-1</sup>, in 500 μL of PBS containing 0.5% hydroxyethyl cellulose) was taken up by oral gavage. A 660 nm laser irradiation (155 mW cm<sup>-2</sup>, 2 min) was performed for each group. The tumor sizes and mice body weights were measured every day, and the tumor volume was defined as  $V = ((\text{length}) \times (\text{width})^2)/2$ . Relative body weight was defined as  $M/M_0$  ( $M_0$  is the starting body weight). On the 15th day, mice were sacrificed, and their hearts, livers, spleens, lungs, kidneys, and tumors were collected for further examination.

## ASSOCIATED CONTENT

### Supporting Information

The Supporting Information is available free of charge on the ACS Publications website at DOI: 10.1021/acsnano.8b02977.

Experimental details, materials and measurements, synthesis of nanoparticles, SDS page, fluorescent quenching experiment, ROS production, glucose/lactate measurement, wound healing assay, distribution studies, and animal experiments (PDF)

## AUTHOR INFORMATION

### Corresponding Author

\*E-mail: xz-zhang@whu.edu.cn.

### ORCID

Xian-Zheng Zhang: 0000-0001-6242-6005

### Author Contributions

<sup>§</sup>D. Zheng and B. Li contributed equally to this work.

### Notes

The authors declare no competing financial interest.

## ACKNOWLEDGMENTS

This work was supported by the National Natural Science Foundation of China (51690152 and 21721005).

## REFERENCES

- Hanahan, D.; Weinberg, R. A. Hallmarks of Cancer: The Next Generation. *Cell* **2011**, *144*, 646–674.
- Gilkes, D. M.; Semenza, G. L.; Wirtz, D. Hypoxia and the Extracellular Matrix: Drivers of Tumour Metastasis. *Nat. Rev. Cancer* **2014**, *14*, 430–439.
- Nakazawa, M. S.; Keith, B.; Simon, M. C. Oxygen Availability and Metabolic Adaptations. *Nat. Rev. Cancer* **2016**, *16*, 663–673.
- Hirschhaeuser, F.; Sattler, U. G. A.; Mueller-Klieser, W. Lactate: A Metabolic Key Player in Cancer. *Cancer Res.* **2011**, *71*, 6921–6925.
- de Palma, M.; Biziato, D.; Petrova, T. V. Microenvironmental Regulation of Tumour Angiogenesis. *Nat. Rev. Cancer* **2017**, *17*, 457–474.
- Zheng, X. C.; Tang, H.; Xie, C.; Zhang, J. L.; Wu, W.; Jiang, X. Q. Tracking Cancer Metastasis *in Vivo* by Using an Iridium-Based Hypoxia-Activated Optical Oxygen Nanosensor. *Angew. Chem., Int. Ed.* **2015**, *54*, 8094–8099.
- Chauhan, V. P.; Stylianopoulos, T.; Martin, J. D.; Popovic, Z.; Chen, O.; Kamoun, W. S.; Bawendi, M. G.; Fukumura, D.; Jain, R. K. Normalization of Tumour Blood Vessels Improves the Delivery of Nanomedicines in a Size-Dependent Manner. *Nat. Nanotechnol.* **2012**, *7*, 383–388.
- Cantelmo, A. R.; Conradi, L. C.; Brajic, A.; Goveia, J.; Kalucka, J.; Pircher, A.; Chaturvedi, P.; Hol, J.; Thienpont, B.; Teuwen, L. A.; Schoors, S.; Boeckx, B.; Vriens, J.; Kuchnio, A.; Veys, K.; Cruys, B.; Finotto, L.; Treps, L.; Stav-Noraas, T. E.; Bifari, F.; et al. Inhibition of the Glycolytic Activator PFKFB3 in Endothelium Induces Tumor Vessel Normalization, Impairs Metastasis, and Improves Chemotherapy. *Cancer Cell* **2016**, *30*, 968–985.
- Mazzone, M.; Dettori, D.; de Oliveira, R. L.; Loges, S.; Schmidt, T.; Jonckx, B.; Tian, Y. M.; Lanahan, A. A.; Pollard, P.; de Almodovar, C. R.; De Smet, F.; Vinckier, S.; Aragones, J.; Debackere, K.; Lutun, A.; Wyna, S.; Jordan, B.; Pisacane, A.; Gallez, B.; Lampugnani, M. G.; et al. Heterozygous Deficiency of PHD2 Restores Tumor Oxygenation and Inhibits Metastasis *via* Endothelial Normalization. *Cell* **2009**, *136*, 839–851.
- Brenner, M. K.; Gottschalk, S.; Leen, A. M.; Vera, J. F. Is Cancer Gene Therapy an Empty Suit? *Lancet Oncol.* **2013**, *14*, E447–E456.
- Jain, R. K. Normalization of Tumor Vasculature: An Emerging Concept in Antiangiogenic Therapy. *Science* **2005**, *307*, 58–62.
- Chen, Q.; Feng, L. Z.; Liu, J. J.; Zhu, W. W.; Dong, Z. L.; Wu, Y. F.; Liu, Z. Intelligent Albumin-MnO<sub>2</sub> Nanoparticles as pH-/H<sub>2</sub>O<sub>2</sub>-Responsive Dissociable Nanocarriers to Modulate Tumor Hypoxia for Effective Combination Therapy. *Adv. Mater.* **2016**, *28*, 7129–7136.
- Cheng, H.; Zhu, J.-Y.; Li, S.-Y.; Zeng, J.-Y.; Lei, Q.; Chen, K.-W.; Zhang, C.; Zhang, X.-Z. An O<sub>2</sub> Self-Sufficient Biomimetic Nanoplat-

- form for Highly Specific and Efficient Photodynamic Therapy. *Adv. Funct. Mater.* **2016**, *26*, 7847–7860.
- (14) Li, S. Y.; Cheng, H.; Xie, B. R.; Qiu, W. X.; Zeng, J. Y.; Li, C. X.; Wan, S. S.; Zhang, L.; Liu, W. L.; Zhang, X. Z. Cancer Cell Membrane Camouflaged Cascade Bioreactor for Cancer Targeted Starvation and Photodynamic Therapy. *ACS Nano* **2017**, *11*, 7006–7018.
- (15) Huang, C. C.; Chia, W. T.; Chung, M. F.; Lin, K. J.; Hsiao, C. W.; Jin, C.; Lim, W. H.; Chen, C. C.; Sung, H. W. An Implantable Depot That Can Generate Oxygen *in Situ* for Overcoming Hypoxia-Induced Resistance to Anticancer Drugs in Chemotherapy. *J. Am. Chem. Soc.* **2016**, *138*, 5222–5225.
- (16) Zheng, D. W.; Li, B.; Li, C. X.; Fan, J. X.; Lei, Q.; Li, C.; Xu, Z. S.; Zhang, X. Z. Carbon-Dot-Decorated Carbon Nitride Nanoparticles for Enhanced Photodynamic Therapy against Hypoxic Tumor *via* Water Splitting. *ACS Nano* **2016**, *10*, 8715–8722.
- (17) Zheng, D. W.; Li, B.; Li, C. X.; Xu, L.; Fan, J. X.; Lei, Q.; Zhang, X. Z. Photocatalyzing CO<sub>2</sub> to CO for Enhanced Cancer Therapy. *Adv. Mater.* **2017**, *29*, 3822.
- (18) Zheng, D. W.; Chen, Y.; Li, Z. H.; Xu, L.; Li, C. X.; Li, B.; Fan, J. X.; Cheng, S. X.; Zhang, X. Z. Optically-Controlled Bacterial Metabolite for Cancer Therapy. *Nat. Commun.* **2018**, *9*, 1680.
- (19) Barber, J. A Mechanism for Water Splitting and Oxygen Production in Photosynthesis. *Nat. Plants* **2017**, *3*, 17041.
- (20) Wang, Y. X.; Li, S. L.; Liu, L. B.; Lv, F. T.; Wang, S. Conjugated Polymer Nanoparticles to Augment Photosynthesis of Chloroplasts. *Angew. Chem., Int. Ed.* **2017**, *56*, 5308–5311.
- (21) Li, Z.; Wang, W. Y.; Ding, C. M.; Wang, Z. L.; Liao, S. C.; Li, C. Biomimetic Electron Transport *via* Multiredox Shuttles from Photosystem II to a Photoelectrochemical Cell for Solar Water Splitting. *Energy Environ. Sci.* **2017**, *10*, 765–771.
- (22) Bassi, R.; Hoyerhansen, G.; Barbato, R.; Giacometti, G. M.; Simpson, D. J. Chlorophyll-Proteins of the Photosystem-II Antenna System. *J. Biol. Chem.* **1987**, *262*, 13333–13341.
- (23) Yang, Y. J.; Huang, J.; Yang, X. H.; Quan, K.; Wang, H.; Ying, L.; Xie, N. L.; Ou, M.; Wang, K. M. FRET Nanoflares for Intracellular mRNA Detection: Avoiding False Positive Signals and Minimizing Effects of System Fluctuations. *J. Am. Chem. Soc.* **2015**, *137*, 8340–8343.
- (24) Wang, W. Y.; Chen, J.; Li, C.; Tian, W. M. Achieving Solar Overall Water Splitting with Hybrid Photosystems of Photosystem II and Artificial Photocatalysts. *Nat. Commun.* **2014**, *5*, 4647.
- (25) Wilson, W. R.; Hay, M. P. Targeting Hypoxia in Cancer Therapy. *Nat. Rev. Cancer* **2011**, *11*, 393–410.
- (26) Lei, Q.; Wang, S. B.; Hu, J. J.; Lin, Y. X.; Zhu, C. H.; Rong, L.; Zhang, X. Z. Stimuli-Responsive “Cluster Bomb” for Programmed Tumor Therapy. *ACS Nano* **2017**, *11*, 7201–7214.
- (27) Lim, J. B.; Huang, B. K.; Deen, W. M.; Sikes, H. D. Analysis of the Lifetime and Spatial Localization of Hydrogen Peroxide Generated in the Cytosol Using a Reduced Kinetic Model. *Free Radical Biol. Med.* **2015**, *89*, 47–53.
- (28) Faubert, B.; Li, K. Y.; Cai, L.; Hensley, C. T.; Kim, J.; Zacharias, L. G.; Yang, C. D.; Do, Q. N.; Doucette, S.; Burguete, D.; Li, H.; Huet, G.; Yuan, Q.; Wigal, T.; Butt, Y.; Ni, M.; Torrealba, J.; Oliver, D.; Lenkinski, R. E.; Malloy, C. R.; et al. Lactate Metabolism in Human Lung Tumors. *Cell* **2017**, *171*, 358–371.
- (29) Zheng, D. W.; Lei, Q.; Zhu, J. Y.; Fan, J. X.; Li, C. X.; Li, C.; Xu, Z. S.; Cheng, S. X.; Zhang, X. Z. Switching Apoptosis to Ferroptosis: Metal-Organic Network for High-Efficiency Anticancer Therapy. *Nano Lett.* **2017**, *17*, 284–291.
- (30) Liberti, M. V.; Dai, Z. W.; Wardell, S. E.; Baccile, J. A.; Liu, X. J.; Gao, X.; Baldi, R.; Mehrmohamadi, M.; Johnson, M. O.; Madhukar, N. S.; Shestov, A. A.; Chio, I. I. C.; Elemento, O.; Rathmell, J. C.; Schroeder, F. C.; McDonnell, D. P.; Locasale, J. W. A Predictive Model for Selective Targeting of the Warburg Effect through GAPDH Inhibition with a Natural Product. *Cell Metab.* **2017**, *26*, 648–659.
- (31) Fabregat, A.; Sidiropoulos, K.; Garapati, P.; Gillespie, M.; Hausmann, K.; Haw, R.; Jassal, B.; Jupe, S.; Korninger, F.; McKay, S.; Matthews, L.; May, B.; Milacic, M.; Rothfels, K.; Shamovsky, V.; Webber, M.; Weiser, J.; Williams, M.; Wu, G. M.; Stein, L.; et al. The Reactome Pathway Knowledgebase. *Nucleic Acids Res.* **2016**, *44*, D481–D487.
- (32) Chung, K.; Wallace, J.; Kim, S. Y.; Kalyanasundaram, S.; Andalman, A. S.; Davidson, T. J.; Mirzabekov, J. J.; Zalocusky, K. A.; Mattis, J.; Denisin, A. K.; Pak, S.; Bernstein, H.; Ramakrishnan, C.; Grosenick, L.; Gradinaru, V.; Deisseroth, K. Structural and Molecular Interrogation of Intact Biological Systems. *Nature* **2013**, *497*, 332–337.
- (33) Lim, S.; Liu, H.; da Silva, L. M.; Arora, R.; Liu, Z. X.; Phillips, J. B.; Schmitt, D. C.; Vu, T.; McClellan, S.; Lin, Y. F.; Lin, W. S.; Piazza, G. A.; Fodstad, O.; Tan, M. Immunoregulatory Protein B7-H3 Reprograms Glucose Metabolism in Cancer Cells by ROS-Mediated Stabilization of HIF1 Alpha. *Cancer Res.* **2016**, *76*, 2231–2242.
- (34) Schmieder, A. H.; Wang, K. Z.; Zhang, H. Y.; Senpan, A.; Pan, D. P. J.; Keupp, J.; Caruthers, S. D.; Wickline, S. A.; Shen, B. Z.; Wagner, E. M.; Lanza, G. M. Characterization of Early Neovascular Response to Acute Lung Ischemia Using Simultaneous F-19/H-1 MR Molecular Imaging. *Angiogenesis* **2014**, *17*, 51–60.
- (35) Gratton, J. P.; Lin, M. I.; Yu, J.; Weiss, E. D.; Jiang, Z. J.; Fairchild, T. A.; Iwakiri, Y.; Groszmann, R.; Claffey, K. P.; Cheng, Y. C.; Sessa, W. C. Selective Inhibition of Tumor Microvascular Permeability by Cavtratin Blocks Tumor Progression in Mice. *Cancer Cell* **2003**, *4*, 31–39.
- (36) Yamada, K.; Saito, M.; Matsuoka, H.; Inagaki, N. A Real-Time Method of Imaging Glucose Uptake in Single, Living Mammalian Cells. *Nat. Protoc.* **2007**, *2*, 753–762.
- (37) Allen, E.; Mievil, P.; Warren, C. M.; Saghafinia, S.; Li, L.; Peng, M. W.; Hanahan, D. Metabolic Symbiosis Enables Adaptive Resistance to Anti-Angiogenic Therapy That Is Dependent on mTOR Signaling. *Cell Rep.* **2016**, *15*, 1144–1160.
- (38) Groussard, C.; Morel, I.; Chevanne, M.; Monnier, M.; Cillard, J.; Delamarche, A. Free Radical Scavenging and Antioxidant Effects of Lactate Ion: An *in Vitro* Study. *J. Appl. Physiol.* **2000**, *89*, 169–175.
- (39) Choi, H. Y.; Lee, J. H.; Jegal, K. H.; Cho, I. J.; Kim, Y. W.; Kim, S. C. Oxyresveratrol Abrogates Oxidative Stress by Activating ERK-Nrf2 Pathway in the Liver. *Chem.-Biol. Interact.* **2016**, *245*, 110–121.
- (40) Kantamneni, H.; Zevon, M.; Donzanti, M. J.; Zhao, X. Y.; Sheng, Y.; Barkund, S. R.; McCabe, L. H.; Banach-Petrosky, W.; Higgins, L. M.; Ganesan, S.; Riman, R. E.; Roth, C. M.; Tan, M. C.; Pierce, M. C.; Ganapathy, V.; Moghe, P. V. Surveillance Nanotechnology for Multi-Organ Cancer Metastases. *Nat. Biomed. Eng.* **2017**, *1*, 993–1003.
- (41) Wang, C.; Sun, W. J.; Wright, G.; Wang, A. Z.; Gu, Z. Inflammation-Triggered Cancer Immunotherapy by Programmed Delivery of CpG and Anti-PD1 Antibody. *Adv. Mater.* **2017**, *29*, 8912–8920.
- (42) Li, S.-Y.; Cheng, H.; Xie, B.-R.; Qiu, W.-X.; Li, C.-X.; Li, B.; Cheng, H.; Zhang, X.-Z. Mitochondria Targeted Cancer Therapy Using Ethidium Derivatives. *Mater. Today Chem.* **2017**, *6*, 34–44.
- (43) Qian, H.; Liu, B.; Jiang, X. Application of Nanomaterials in Cancer Immunotherapy. *Mater. Today Chem.* **2018**, *7*, 53–64.